



# Rapid Synthesis of Bismuth MOF @Carbon Nanotube Composite by microwave-assisted Solvothermal for Photodegrading RhB

Huynh Thanh Quang<sup>1</sup> · Hoang Ai Le Pham<sup>1</sup> · Nguyen Van Cuong<sup>1</sup> · Huu Phuc Dang<sup>2</sup> · Nguyen Thi Hong Anh<sup>3</sup>

Accepted: 7 June 2024 / Published online: 4 July 2024

© The Author(s), under exclusive licence to Springer Science+Business Media, LLC, part of Springer Nature 2024

## Abstract

We synthesized a bismuth-MOFs@CNTs (BiBTC@CNTs) catalyst using a microwave-assisted solvothermal method. The mass ratios of CNTs and BiBTC varied from 0 to 2, 5, and 10% (denoted as BiBTC@CNTs-x, x=0 to 2, 5, and 10). The characteristics of the catalyst were determined by X-ray diffraction (XRD), Fourier transform infrared (FT-IR) spectroscopy, scanning electron microscopy (SEM), X-ray photoelectron spectroscopy (XPS), and diffuse reflectance spectroscopy (UV-Vis DRS). The catalytic activity of the material was tested by photodegradation of rhodamine B. The structure of BiBTC@CNTs-x displayed a UU-200 and CNT structure with rod-shaped interweaving between the CNT fibers. The results indicated that BiBTC@CNTs-2 had the most significant ability to degrade RhB, achieving 98% degradation in 180 min. The increased separation of electron-hole pairs via a built-in electric field between CNT and BiBTC is responsible for the improved photocatalytic degradation of RhB, as observed in the XPS spectrum, transient photocurrent response, electrochemical impedance spectroscopy (EIS), and Mott-Schottky plots. In addition, the catalyst mass, dye concentration, pH of the medium, and radical scavengers were investigated. Furthermore, free radicals ( $O^{2-}$ ) and electrons ( $e^-$ ) played the primary and most influential role in the photocatalytic degradation of both dyes, with a minor contribution from the photogenerated holes ( $h^+$ ). Kinetic study of the dye degradation process followed a first-order kinetic model.

**Keywords** BiBTC@CNT · Rhodamine B · Metal-organic framework · Photocatalyst

## 1 Introduction

Every year, the textile dyeing industry releases approximately 200,000 tons of synthetic dyes, comprising approximately 17–20% of industrial wastewater, causing water pollution and directly affecting human health [1]. To solve these environmental problems, many research groups have

developed effective methods and advanced materials to treat wastewater dyes with high efficiency and reusability. In particular, the advanced oxidation method (AOP) is based on the formation of free radicals that act as oxidizing-reducing agents to break down the structure of pollutants and make materials less harmful to the environment [2]. Among them, advanced photocatalytic oxidation processes are an effective advanced oxidation process widely researched to solve dye pollution problems owing to their fast reaction rates, strong oxidation capability, and low cost compared to non-photolytic AOP [3]. Traditional photocatalytic semiconductor materials, such as oxides  $TiO_2$ ,  $ZnO$ ,  $SnO_2$ ,  $Cu_2O$ ,  $WO_3$ , and  $Fe_2O_3$  [4–8], have been extensively studied to enhance the photodegradation ability of dyes in wastewater. These semiconductor materials absorb photons with energies equal to or higher than their bandgap, generating electron-hole pairs ( $e/h^+$ ). These electron-hole pairs can move to form reactive species such as hydroxyl radicals ( $\bullet OH$ ) or superoxide radical anions ( $\bullet O^{2-}$ ), which can decompose many dangerous organic substances [9, 10].

✉ Huu Phuc Dang  
danghuuphuc@iuh.edu.vn

✉ Nguyen Thi Hong Anh  
anhnh@huit.edu.vn

<sup>1</sup> Faculty of Chemical Engineering, Industrial University of Ho Chi Minh City, Ho Chi Minh City 70000, Vietnam

<sup>2</sup> Faculty of Fundamental Science, Industrial University of Ho Chi Minh City, Ho Chi Minh City 70000, Vietnam

<sup>3</sup> Faculty of Chemical Engineering, Ho Chi Minh City University of Industry and Trade, 140 Le Trong Tan Street, Tay Thanh Ward, Tan Phu District, Ho Chi Minh City 70000, Vietnam

Metal-organic frameworks (MOFs) are a novel category of porous substances that comprise organic ligands and metal sites. These materials are gaining attention because of their potential applications in gas adsorption and separation, drug delivery, photocatalysis, sensing, and photocatalysis. Researchers have increasingly drawn attention to certain metal-organic frameworks (MOFs) in recent years as a promising class of porous catalysts. For example, Fe-MOFs [11], Zr-MOFs [12], Zn-MOFs [13], and Bi-MOFs [14–17] have garnered significant interest. Among these, Bi-MOFs have been the least explored. Bismuth, the central metal in Bi-MOFs, is non-toxic and possesses a flexible coordination geometry, with a 3-dimensional frame structure and adjustable pore size. The  $\text{Bi}^{3+}$  metal center can act as an acidic Lewis site in the adsorption and catalysis of various organic reactions [18]. Several novel Bi-MOF structures, such as UU-200 (Uppsala University) [19], CAU-17 (Christian Albrechts University) [20], CAU-33 [21], Bi-BTC [22, 23], and Bi-BDC [24] have been reported as photocatalysts. Among these, trimesate-based Bi-MOFs are not only diverse in structure but also highly stable and easy to prepare for photocatalytic applications. Vinh et al. investigated the influence of solvent (DMF and MeOH) on the structure and photodegradation of RhB of bismuth and trimesic acid [25]. The decomposition efficiencies of RhB were: Bi-BTC-DMF (13.24%) was lower than Bi-BTC-MeOH (81.49%), and Bi-BTC-MDF/MeOH (95.06%) after 100 min of illumination. Recently, H. Qin et al. enhanced the absorption of visible light in CAU17 by growing it on cotton fabrics, achieving a removal rate of 98.77% for RhB after 180 min of light exposure [26]. However, the photocatalytic oxidation properties of pure Bi-MOFs remain inadequate, and their poor conductivity and low visible-light response often hinder their photocatalytic performance [27]. Currently, the improved use of heterojunction composites composed of narrow-gap semiconductors improves the visible-light response and efficiency of transport and separation of photogenerated carriers [28, 29]. Lin Yang et al. synthesized the  $\text{Bi}_2\text{WO}_6/\text{CAU-17}$  structure for the photodegradation of RhB, Orange II, Methylene Blue, and phenol. The results showed that the decomposition efficiency reached 80% for RhB, 70% for Org II after 60 min, and 48.1% for phenol after 120 min [30]. Feihu Zhang et al. studied  $\text{AgI}/\text{CA-17}$  photocatalytic of Methyl Orange (MO), Tetracycline Hydrochloride (TC), and RhB under a 500 W Xenon lamp for 70 min. The efficiencies reached 96.7, 81.3, and 50.3% for RhB, TC, and MO, respectively [31]. In addition to the above materials, carbon materials possess high electrical conductivity and have been combined with MOFs to form synthetic materials, enhancing the electrochemical activity and electrical conductivity [25–27]. Carbon nanotubes have unique properties such as outstanding electrical and thermal

conductivities and a large specific surface area [32]. CNTs can increase stability and reduce the recombination of electrons with holes when combined with other semiconductor materials [33]. Furthermore, the large specific surface area of CNTs can enhance the adsorption capacity of MOFs, thereby promoting faster photocatalysis [34]. Therefore, the BiBTC@CNT composites are promising materials for increasing the efficiency of photodegradation.

This study utilized a microwave-assisted solvothermal method to modify CNTs on BiBTC at various mass percentages, which were subsequently analyzed using X-ray diffraction (XRD), Fourier-transform infrared (FT-IR) spectroscopy, scanning electron microscopy (SEM), diffuse reflectance spectroscopy (DRS), and ultraviolet-visible (UV-Vis) absorption spectroscopy. The objective of this study was to investigate the influence of changes in the CNT mass percentage on the light absorption property, separation of  $e/h+$  pairs, and the subsequent effect on the photocatalytic performance of the as-synthesized MOFs during the photocatalytic decomposition of rhodamine B (RhB).

## 2 Experiment

### 2.1 Synthesis of Materials

#### 2.1.1 Material

Trimesic acid ( $\text{H}_3\text{BTC}$ ,  $\geq 98\%$ ), bismuth (III) nitrate pentahydrate ( $\text{Bi}(\text{NO}_3)_3 \cdot 5\text{H}_2\text{O}$ ,  $\geq 99.5\%$ ), 1,4-Benzoquinone ( $\text{C}_6\text{H}_4\text{O}_2$ ), and tert-butanol ( $(\text{CH}_3)_3\text{COH}$ ,  $\geq 99.5\%$ ) were obtained from Sigma-Aldrich Co. Ltd. Methanol ( $\text{MeOH}$ ,  $\text{CH}_4\text{O}$ ,  $\geq 99.5\%$ ), N, N-dimethylformamide (DMF,  $\text{C}_3\text{H}_7\text{NO}$ , 99%), AR (Xilong Chemical, Methanol (99%, AR), and rhodamine B dye (RhB,  $\text{C}_{28}\text{H}_{31}\text{ClN}_2\text{O}_3$ , 95%) were purchased from Xilong Scientific Co., Ltd. Deionized water was obtained from Yamato (Japan). All the commercial reagents and solvents were used without additional purification.

#### 2.1.2 Synthesis of BiBTC@CNTs and BiBTC Materials

First, 0.07485 g of  $\text{Bi}(\text{NO}_3)_3 \cdot 5\text{H}_2\text{O}$  was dissolved in 15 mL of MeOH/DMF solvent, volume/volume (1:1, v/v), to obtain solution (A) 0.3647 g  $\text{H}_3\text{BTC}$  was dissolved in 15 mL of MeOH/DMF solvent (1:1, v/v) to obtain solution (B) CNTs were dispersed in 15 mL of MeOH/DMF solvent (1:1, v/v) to obtain solution (C) All the solutions were stirred and sonicated for 60 min. The mixture of solutions A, B, and C was then stirred for 60 min and sonicated for 60 min to evenly disperse the substances. The resulting solution was placed in a 250-mL flask and heated in a microwave for

90 min at 400 W (Sharp, model R-201VN-W). The mixture was washed twice with MeOH to remove DMF and then dried at 80°C to get the BiBTC@CNT powder. In this study, BiBTC@CNT composite samples were prepared by changing the amount of CNTs in  $\text{Bi}(\text{NO}_3)_3 \cdot 5\text{H}_2\text{O}$  by 2, 5, and 10%. The labels are named BiBTC@CNTs-2, BiBTC@CNTs-5, and BiBTC@CNTs-10. In addition, a BiBTC sample without CNT was also fabricated for comparison (See Scheme1).

## 2.2 Characteristics of the Catalyst

X-ray diffraction was carried out using a Shimadzu 6100 diffractometer equipped with a high-speed detector and a scanning speed of 6 degrees per second. High-resolution scanning Electron Microscopy (FESEM) and energy-dispersive X-ray spectroscopy (EDX) analyses were performed using a JSM-IT500 instrument. Fourier transform infrared spectroscopy (FTIR) in the transmission mode was used to analyze the characteristic bonds and functional groups in the material. UV-Vis diffuse reflectance spectroscopy (Cary 4000 UV-Vis spectrophotometer) was used to obtain adsorption spectra of the catalysts. The chemical composition of the surface of the material was analyzed using X-ray photoelectron spectroscopy (XPS) on an AXIS Ultra DLD machine. The pH of the solvent was measured using a Thermo Fisher Scientific meter (Orion Star A211). Mott-Schottky plots, photocurrent curves, and Nyquist plots were obtained using a CHI 650E electrochemical workstation with a three-electrode cell in a 0.1 M  $\text{Na}_2\text{SO}_4$  electrolyte solution.

## 2.3 Photocatalytic Degradation of RhB

The experiment on the catalytic optical degradation of RhB was carried out in a dark chamber using 60 W LEDs (LEDs) to act as a light source ( $100 \text{ mW}/\text{cm}^2$ ) in a two-layer

reactor container with a continuous cooling water flow moving between the two layers to stabilize the temperature of the reaction while maintaining the temperature at room temperature.

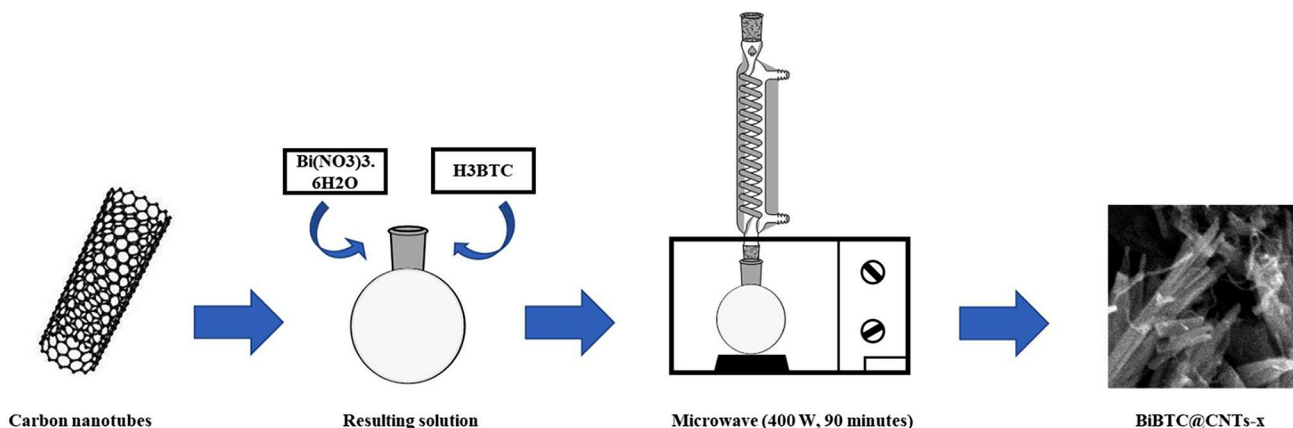
Rhodamine B (RhB) was used for the water contaminant tests. The catalyst (10 mg) and the RhB solution (50 mL) were mixed in a reaction vessel. The solution was then stirred in the dark for 60 min to balance adsorption and desorption. This solution underwent a photocatalytic reaction for 180 min, and 5 ml of samples were taken every 30 min to determine the concentration and return to the reactor to continue the photocatalytic process. The samples were centrifuged at 5000 rpm to remove solids and the optical density of the liquid solution was measured at  $\lambda_{\text{max}} = 554 \text{ nm}$ . In addition, the optical density of RhB at the corresponding concentration was determined, as shown in Figure S1. The RhB decomposition efficiency was calculated using the following formula:

$$H = \frac{(C_0 - C_t)}{C_0} \times 100 = \left(1 - \frac{C_t}{C_0}\right) \times 100 \quad (1)$$

where H is the RhB decomposition efficiency,  $C_0$  is the initial concentration of the dye without catalyst, and  $C_t$  is the concentration of the dye at time t.

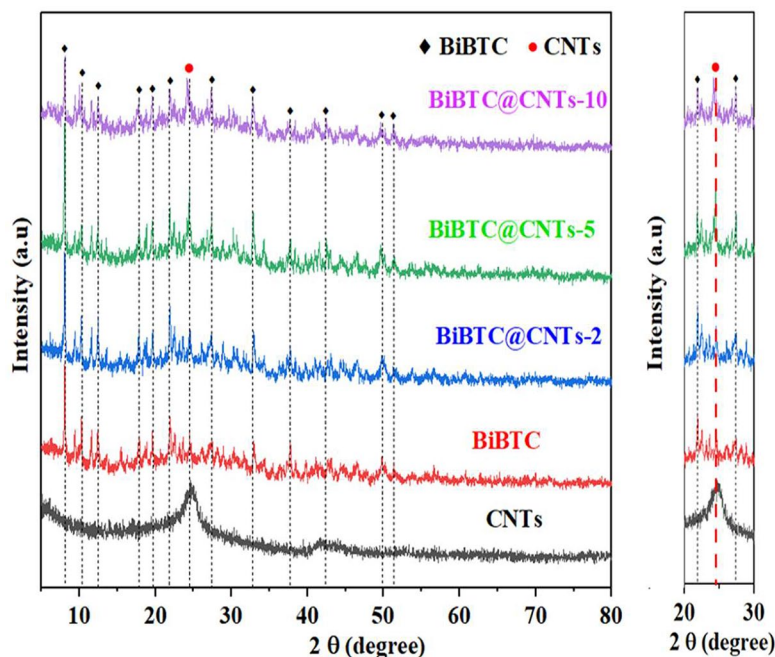
## 3 Results and Discussion

Figure 1 shows the X-ray diffraction patterns of CNTs, BiBTC, BiBTC@CNTs-2, BiBTC@CNTs-5, and BiBTC@CNTs-10. The XRD spectrum of the CNTs shows a characteristic peak at  $2\theta = 24^\circ$ , corresponding to the (002) plane [34]. The XRD spectrum of BiBTC has characteristic peaks at  $2\theta = 8^\circ, 10^\circ, 13^\circ,$  and  $18^\circ$ , related to the (001), (211), (401), and (002) planes. This structure is similar to that of BiBTC synthesized by Deng et al. [35] and is called UU-200

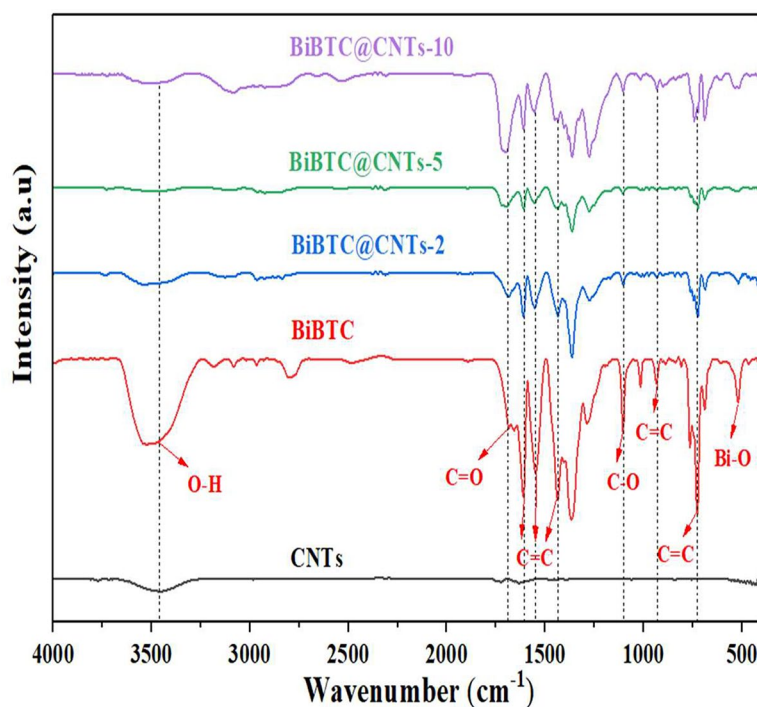


Scheme 1 Synthetic process of BiBTC@CNT

**Fig. 1** XRD patterns of CNTs, BiBTC, BiBTC@CNTs-2, BiBTC@CNTs-5, and BiBTC@CNTs-10 samples, inset XRD patterns in range  $2\theta = 20\text{--}30$



**Fig. 2** FT-IR spectra of CNTs, BiBTC, BiBTC@CNTs-2, BiBTC@CNTs-5, and BiBTC@CNTs-10 samples



(CCDC: 2,103,784) [3]. The spectra of BiBTC@CNTs have simultaneous peaks at  $2\theta = 8^\circ$ ,  $10^\circ$ ,  $13^\circ$ , and  $18^\circ$  for UU-200, and the  $2\theta = 24.8^\circ$  peak of CNTs corresponding to JCPDS card No. 75-2078) [36]. The intensity of the  $2\theta = 24.8^\circ$  peak increased with the increasing weight% of CNTs in the composites. In addition, the X-ray diffraction pattern does not show a significant shift at the peak position.

Figure 2 shows the material bonding characteristics of CNTs, BiBTC, BiBTC@CNTs-2, BiBTC@CNTs-5, and

BiBTC@CNTs-10 using the infrared spectra (FT-IR). The results showed that the characteristic vibrations of BiBTC include Bi-O, C=C, and C=O bonds at positions  $519\text{ cm}^{-1}$ ,  $1549\text{ cm}^{-1}$ , and  $1690\text{ cm}^{-1}$ , respectively [3]. The characteristic peak of CNTs was detected at  $1633\text{ cm}^{-1}$ , which corresponds to the vibration of the C=C bond [34]. The absorption peak at  $3500\text{ cm}^{-1}$  is characterized by H-O vibrations owing to free water molecules in the voids of the material [37].

The morphologies of the synthesized BiBTC and BiBTC@CNTs are shown in Fig. 3. Figure 3a shows that the synthesized BiBTC has a rod-shaped structure with different sizes. Figure 3c shows that the length of UU-200 rods is distributed from 0.5 to 4.5  $\mu\text{m}$ , concentrated in the

range of 1 to 2  $\mu\text{m}$ . Besides, the diameter of BiBTC rods is distributed in the range of 0.2–1.2  $\mu\text{m}$  and concentrated in the range of 0.4–0.6  $\mu\text{m}$  (Fig. 3d). The morphology of BiBTC@CNTs (Fig. 3. b) retained the rod-shaped structure of UU-200, interwoven with the fiber structure of the

**Fig. 3** SEM images of BiBTC (a) and BiBTC@CNTs-2 (b) with corresponding length (c and d) and width (e and f) distribution histograms

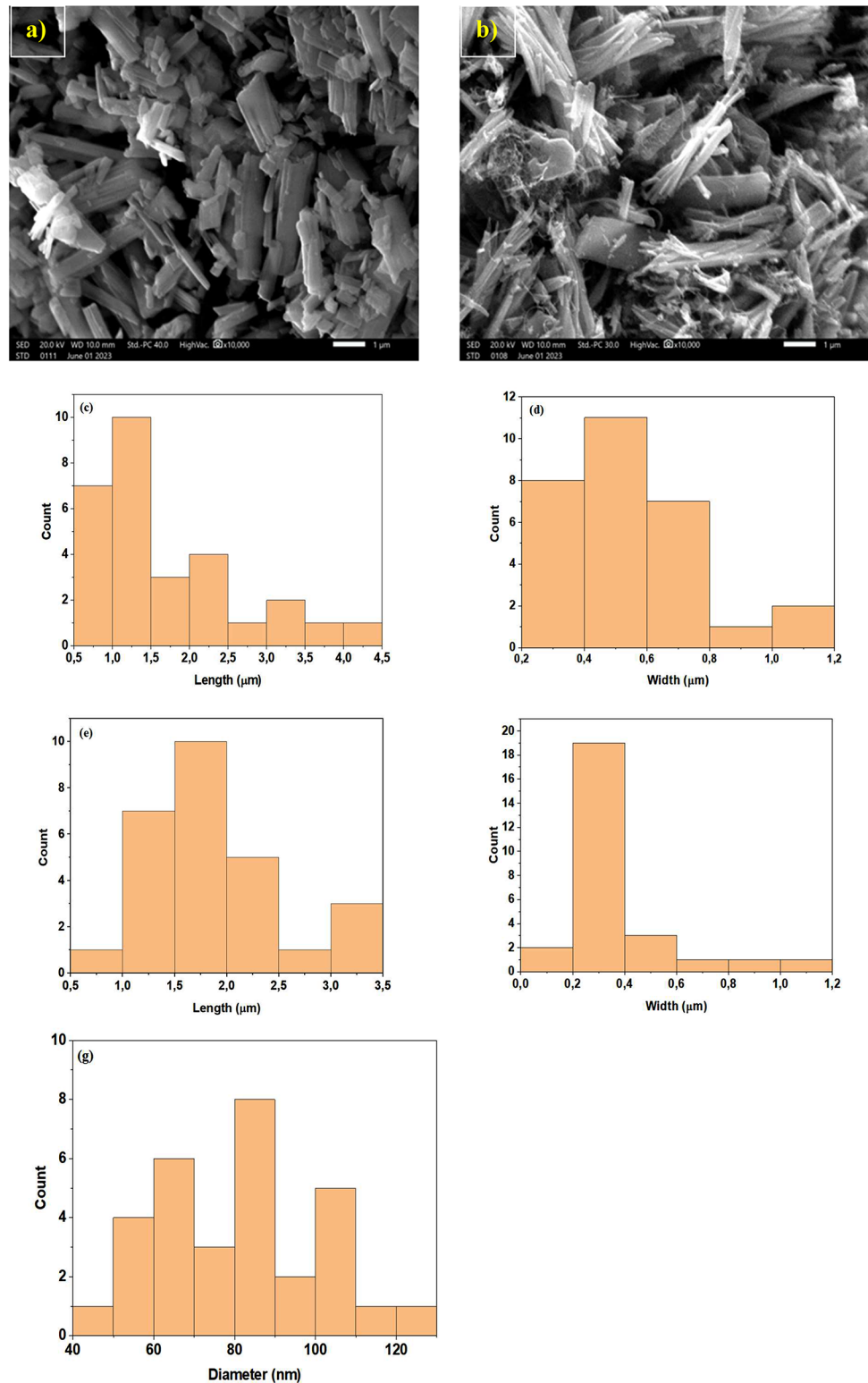


**Fig. 4** Mapping elements Bi, C, and O in BiBTC@CNTs-2

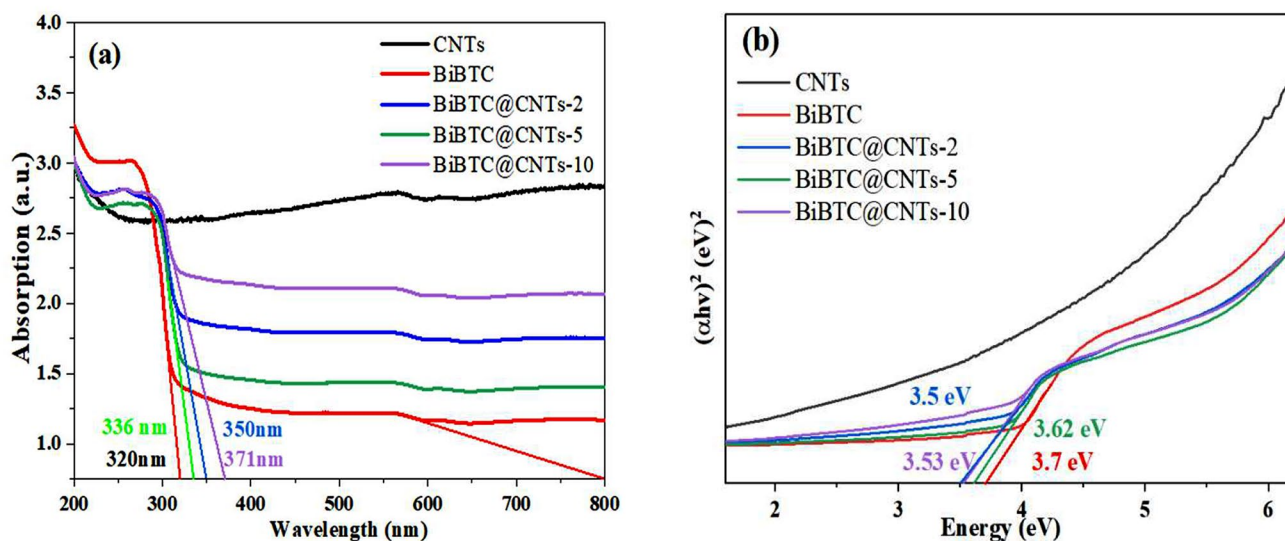
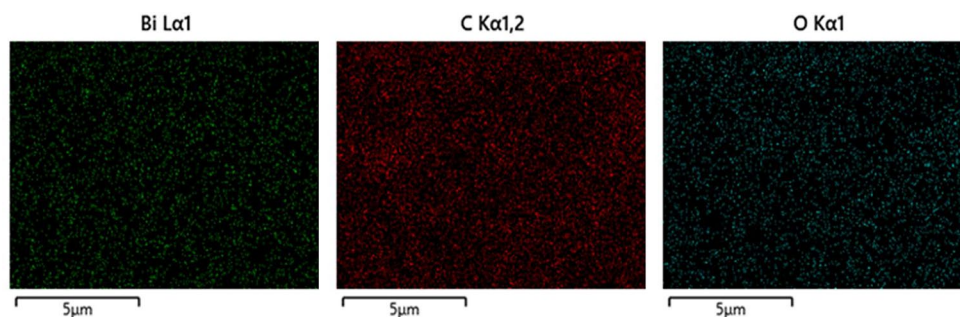


**Fig. 5** (a) UV-Vis/DRS spectrum and (b) bandgap energy of CNTs, BiBTC, and BiBTC@CNTs-x

CNTs. Figure 3f shows that the rods of BiBTC@CNTs have a width distribution in the range of 0.1–1.2  $\mu\text{m}$  and a concentration in the range of 0.2–0.4  $\mu\text{m}$ . The CNTs fibers interwoven between BiBTC had small diameters distributed in the range of 40–130 nm and were concentrated at approximately 80 nm. CNTs fibers interwoven with BiBTC are expected to enhance hole-electron separation without changing the shape of the BiBTC@CNT heterostructure, as observed in a previous study [38].

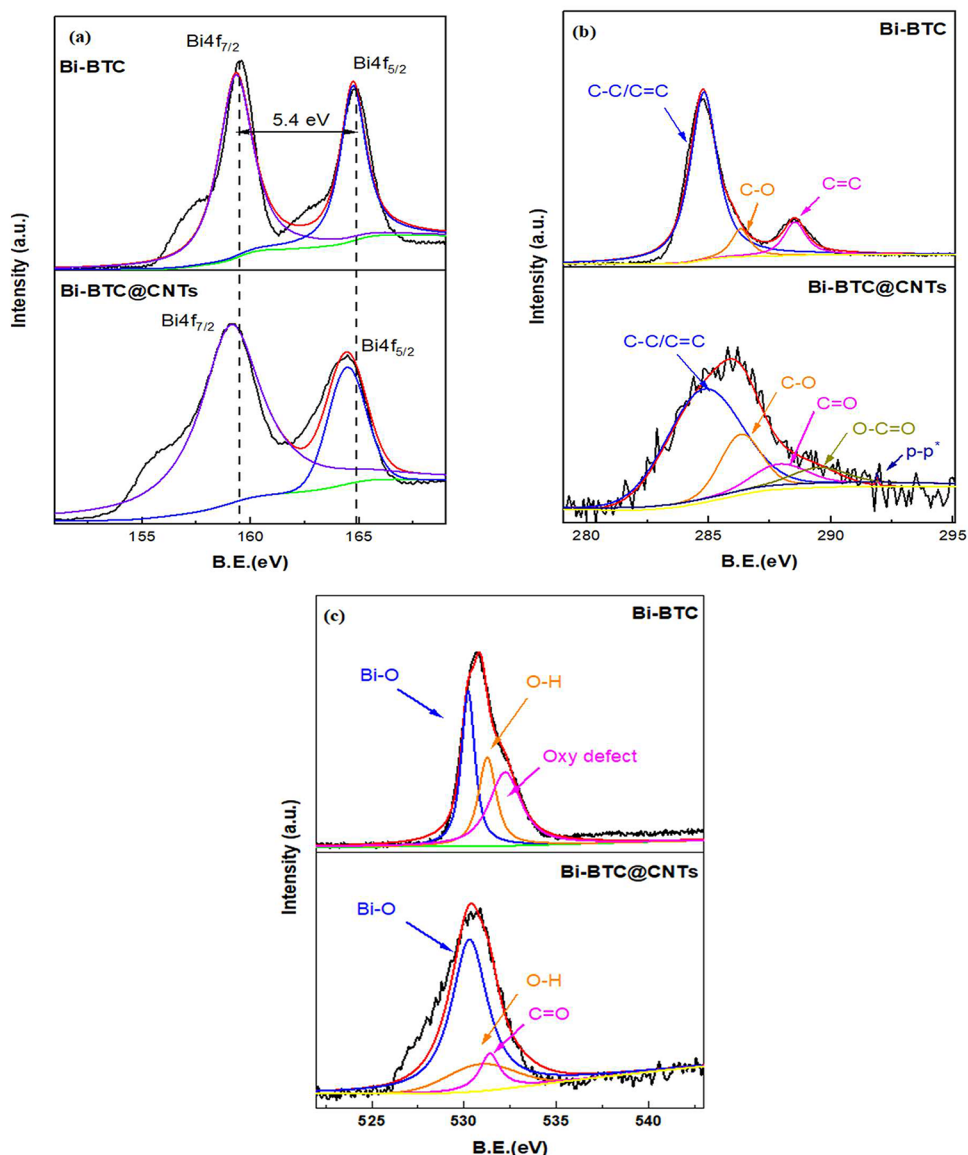
Figure 4 shows the corresponding energy-dispersive X-ray spectroscopy (EDS) measurements of elements in the BiBTC@CNT material. Energy-dispersive X-ray spectroscopy (EDS) measurements revealed the presence of three elements: bismuth (Bi), carbon (C), and oxygen (O) on the surface of the material. Furthermore, elemental mapping using EDS showed a uniform and dense distribution of these three elements across the surface.

Figure 5 shows the optical absorption properties of the BiBTC@CNT composites studied using UV-Vis diffuse reflectance spectroscopy (UV-Vis/DRS). The optical absorption edge of BiBTC is observed at 320 nm, as shown in Fig. 5a [37]. The absorption edge of the BiBTC@CNT

samples had a longer wavelength shift than that of BiBTC because of the CNTs distributed on the surface. These results demonstrate that CNTs can expand the absorption region of the catalyst, allowing it to absorb more light in the visible region. The bandgap energies ( $E_g$ ) of BiBTC, BiBTC@CNTs-2, BiBTC@CNTs-5, and BiBTC@CNTs-10 were calculated from  $(\alpha h\nu)^r$  vs.  $h\nu$ , where  $r=2$  is the direct bandgap, as mentioned in previous studies [20, 39]. Figure 5b shows that the results were recorded at 3.7 eV, 3.5 eV, 3.62 eV, and 3.53 eV, respectively. In addition, CNTs help slow the recombination rate of electron-hole pairs by continuously receiving electrons from the semiconductor [33].

The surface chemical composition and chemical state of the surface elements in the BiBTC@CNTs were analyzed using X-ray photoelectron spectroscopy (XPS), as shown in Fig. 6. Figure 6a shows the binding energy (BE) value of the Bi 4f spectrum of BiBTC@CNTs is around 160 (Bi 4f<sub>7/2</sub>) and 165.4 eV (Bi 4f<sub>5/2</sub>) with different energies (Bi 4f<sub>5/2</sub>–Bi 4f<sub>7/2</sub>) of 5.4 eV, proving that Bi is mainly in the form of Bi (III) [40]. Moreover, the CNTs decorated with BiBTC caused the position of the Bi peak in the BiBTC@

**Fig. 6** XPS spectrum of BiBTC@CNTs-2 and BiBTC with signals of (a) Bi 4f, (b) C 1s, and (c) O 1s



CNTs to shift toward a lower binding energy owing to an increase in the electron cloud density around the Bi atoms, as mentioned in a previous study [5, 41]. The C1s peaks of BiBTC@CNTs (Fig. 6b) can be divided into five main peaks: 284.8, 286.3, 288.9, 289.5, and 291.4 eV [17]. The peak at 284.8 eV was attributed to the C–C/C=C bond of BiBTC and CNTs [42]. The BE at 286.3 and eV correspond to the C–O bonds of BiBTC and CNTs, respectively [42]. The peak at 287.8 eV is characteristic of C=O of BiBTC and on the surfaces of CNTs [42, 43]. The peak at 289.5 eV characterizes the O–C=O bond of UU-200 [44]. The level of 291.9 eV can be attributed to the  $\pi$ – $\pi^*$  satellite bands in CNTs [3]. Meanwhile, the deconvolution of BiBTC C1s peak has C–C/C=C, C–O, and C=C at 284.8, 286.3, and 288.5 eV, respectively [45]. Figure 6c shows the binding energy value of O1s in BiBTC@CNTs recorded at peaks

530.3, 531.4, and 531.1 eV corresponding to the Bi–O, C=O bond bands in the carboxylate Enhanced electrochemical performance of the group and hydroxyl radicals are adsorbed on the surface [45].

The photocatalytic performance of the BiBTC@CNTs was studied using Rhodamine B as an organic pollutant. In this process, BiBTC@CNTs-2 exhibited better activity than BiBTC, as shown in Fig. 7a. However, when the mass ratio of CNTs increased, the photocatalytic activity decreased significantly. The efficiency of RhB degradation by BiBTC and BiBTC@CNTs followed a first-order kinetic reaction model:

$$\ln(C_0/C_t) = kt.$$

where  $k$  is the reaction rate constant ( $\text{min}^{-1}$ ) and  $C_0$  and  $C_t$  correspond to the RhB concentration at times 0 and  $t$ , respectively. The kinetic equations and reaction rate constants are

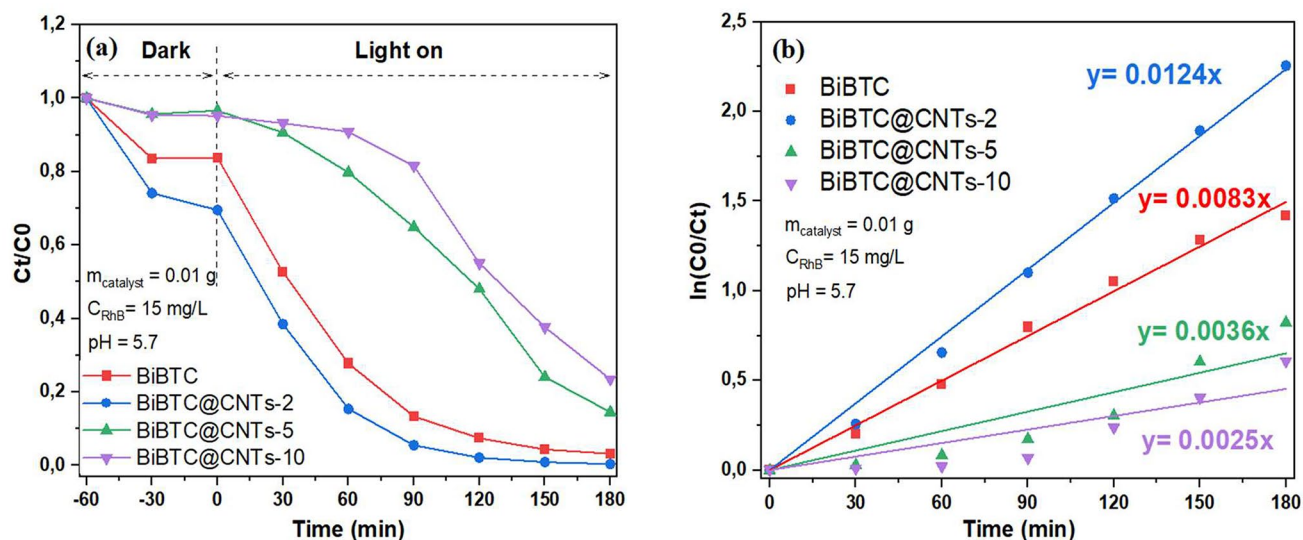


**Fig. 7** (a) Photocatalytic reaction curve under visible light of BiBTC and BiBTC@CNTs-*x* in 180 min. (b) Photocatalytic kinetics of BiBTC and BiBTC@CNTs-*x*

shown in Fig. 7b. The results show that BiBTC@CNTs-2 has the highest reaction rate constant ( $0.0124 \text{ min}^{-1}$ ), 1.5 is more than of BiBTC ( $0.0083 \text{ min}^{-1}$ ), 3.4 times more than BiBTC@CNTs-5 and 4.96 times that of BiBTC@CNTs-10. These results show that combining an appropriate amount of CNTs with BiBTC significantly changes the photocatalytic activity. Although the results show that CNTs are excellent conductors, helping to separate electron and hole pairs [46], CNTs do not exhibit photocatalytic ability under visible light [47]. Therefore, increasing the amount of CNTs can increase the surface coverage and decrease the energy received from the light source, and the RhB molecules are unable to reach the active centers of the catalyst. Consequently, the photocatalytic ability and adsorption capacity of the catalyst were significantly reduced.

#### • Effect of BiBTC@CNTs-2 loading.

This study investigated the effect of loading the BiBTC@CNTs-2 catalyst on RhB degradation performance. Figure 8a shows the experimental samples were prepared with different loadings of BiBTC@CNTs-2 (0.005, 0.01, 0.015, and 0.02 g, respectively). The results showed that The 0.005 g sample had the lowest efficiency (approximately 67%) after 120 min. The samples weighing 0.01 g have the best efficiency, reaching 98%. This study shows that the loading of the catalysts has a significant influence on their photocatalytic ability. This is due to the dispersibility of the material in the environment. In the same volume of solution with the same concentration of RhB, the loading of catalysts is small, and there are not enough active sites to catalyze the decomposition of RhB. However, the loading of the catalysts is too

high, resulting in the formation of large particles, reducing the specific surface area and preventing contact between the RhB molecules and the active substance, thereby reducing the catalytic efficiency of the BiBTC@CNTs-2 material.

To determine the reaction rate constant for RhB decomposition, a kinetic equation was constructed using  $\ln(C_0/C_t)$  and time *t* under the influence of a catalyst, as shown in Fig. 8b. Rhodamine B degradation performance was sorted in the order of corresponding catalyst mass:  $0.01 \text{ g} > 0.015 \text{ g} > 0.02 \text{ g} > 0.005 \text{ g}$ . RhB was almost completely decomposed when using a catalyst mass of 0.01 g. When the catalyst mass was reduced, RhB decomposition efficiency decreased. When the catalyst mass was greater than 0.01 g, the more the catalyst mass increased, the RhB decomposition efficiency gradually decreased. The highest reaction rate when using 0.01 g of material has  $k = 0.0124 \text{ min}^{-1}$  and correlation coefficient  $R^2 = 0.9981$ ; the lowest is when using 0.005 g of material with  $k = 0.0039 \text{ min}^{-1}$  and correlation coefficient  $R^2 = 0.9906$ . According to the results of this study, a catalyst dosage of 10 mg/50 mL RhB was suitable for the catalytic process to proceed quickly and at the most appropriate time.

This study investigated the effect of RhB concentration on the performance of the BiBTC@CNTs-2 catalyst, as shown in Fig. 8c. Four different concentrations of RhB were studied, ranging from 10 ppm to 40 ppm. The results indicate that the degradation rate increased as the RhB concentration decreased. In approximately 120 min, 10 ppm RhB decomposed with high efficiency (98%), whereas 15 ppm RhB took 180 min to completely decompose. Research has shown that the RhB concentration has a great influence on the catalytic activity of BiBTC@CNTs-2; the reaction



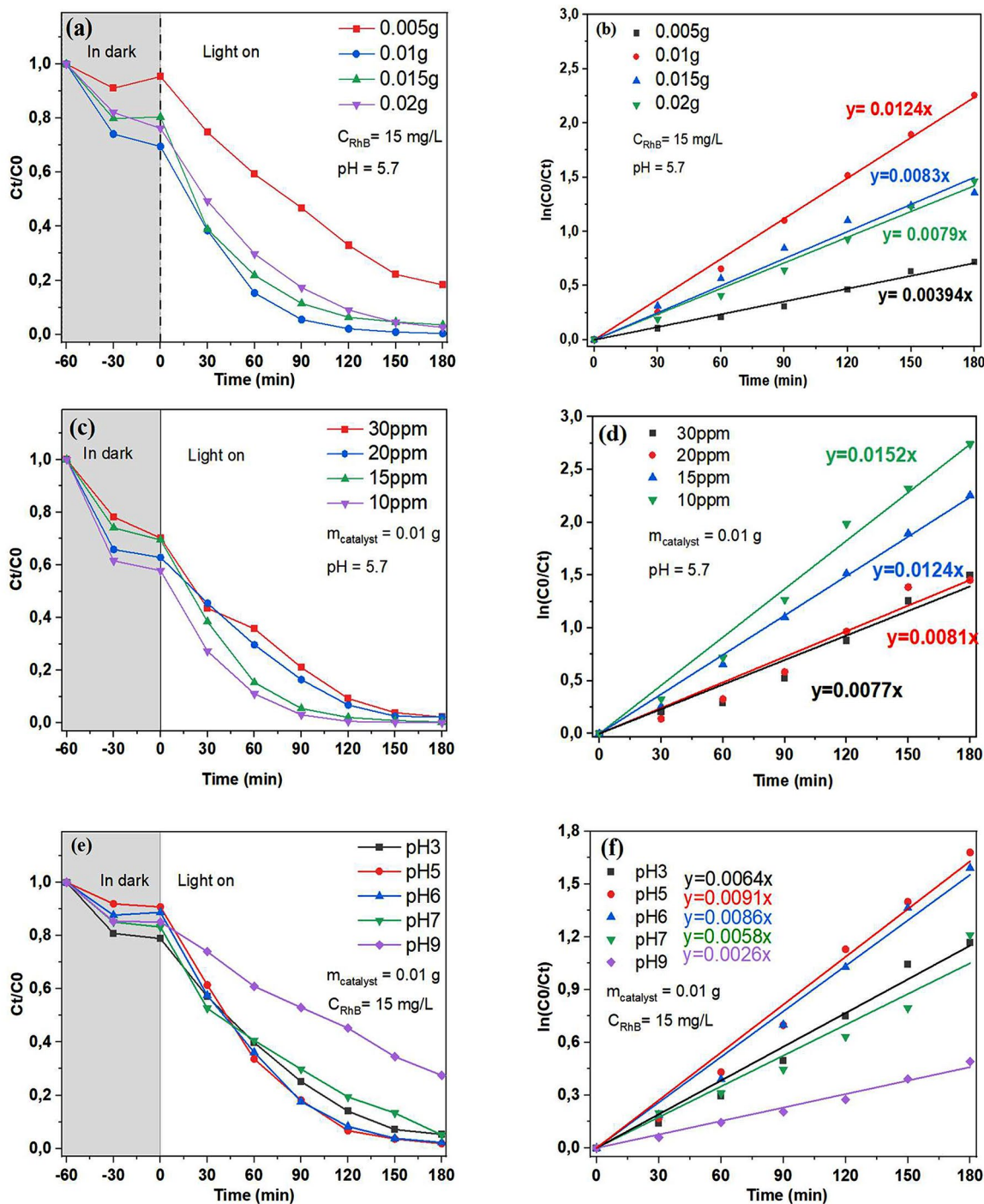


**Fig. 8** The influence of catalyst mass (a), RhB concentration (c), and environmental pH (e) on the ability to decompose RhB; First-order kinetics under the influence of catalyst (b), RhB concentration (d), pH of the environment (f)

rate is slower when the RhB concentration is increased. This can be explained by the porous structure and location of the active center of the catalyst. At low concentrations, RhB molecules are better able to contact the active sites of the material, thereby making the catalytic process faster. At high concentrations, the density of RhB was higher and the

active sites were saturated, leading to a longer loss of time for the photocatalytic decomposition of RhB. In addition, high concentrations cause RhB molecules to easily form large particles, making it difficult to contact the active sites and hindering the contact of other RhB molecules with the active sites.

The kinetic equation  $\ln(C_t/C_0)$  versus time ( $t$ ) was used to determine the kinetics of the photocatalytic degradation of RhB under the influence of RhB concentration. The decomposition rate of Rhodamine B in the survey was as follows: 10 ppm > 15 ppm > 20 ppm > 30 ppm, as shown in Fig. 8d. At concentrations of 15 ppm or lower, RhB was almost completely decomposed. As the RhB concentration increases, the activity of the material gradually decreases. The highest reaction rate was obtained at an RhB concentration of 10 ppm with  $k=0.0152 \text{ min}^{-1}$  and a correlation coefficient  $R^2=0.9952$ . The lowest reaction rate was obtained at an RhB concentration of 30 ppm, with  $k=0.0077 \text{ min}^{-1}$  and correlation coefficient  $R^2=0.9836$ . However, the RhB concentration of 15 ppm had a high reaction rate constant ( $k=0.0124 \text{ min}^{-1}$ ) and a higher correlation coefficient than the experimental sample with an RhB concentration of 10 ppm. From the results of this study, it can be seen that a concentration of 15 ppm is suitable for the catalytic process to proceed quickly and at the most appropriate time.

The pH had a significant influence on the photocatalytic activity of BiBTC@CNTs-2. In this study, a pH-adjusted RhB solution with five different pH values (2, 3, 5, 7, and 9) is investigated. The information provided in Fig. 8e reveals that the effectiveness of the RhB decomposition environment at pH 5 and 6 is greater than that at pH 3, 7, or 9. Specifically, at pH 9, the efficiency of the RhB catalytic degradation process reached only 72.7%. This may be attributed to the interaction between the dye and the catalyst surface, which is influenced by the molecular structure of the dye and isoelectric point (PZC) of the catalyst. The isoelectric point ( $\text{pH}_{\text{pzc}}$ ) of BiBTC@CNTs-2 was 3.5, as depicted in Figure S2. In a pH environment below  $\text{pH}_{\text{pzc}}=3.5$ , the BiBTC@CNTs-2 surface was positively charged, causing the catalyst to repel cationic molecules (RhB dye) in this pH range. However, in a pH environment above  $\text{pH}_{\text{pzc}}=3.5$ , the surface of BiBTC@CNTs-2 was

negatively charged, allowing the catalyst to attract cationic molecules and repel anionic molecules. Nevertheless, as the pH of the environment increased above 9, the surface of the RhB dye molecules became negatively charged in the alkaline region ( $\text{pH} > 7$ ) [48], thereby reducing the adsorption of negatively charged RhB dye molecules. Additionally, the hydroxide ( $\text{OH}^-$ ) ions present in the solution can compete with dye molecules for adsorption sites on the negatively charged catalyst surface, decreasing the overall efficiency of the digestion process.

The addition of free radical scavengers significantly affected the efficiency of the BiBTC@CNT material for the photodegradation of RhB. In this study, four scavengers, BQ (capture  $\bullet\text{O}_2^-$ ),  $\text{Na}_2\text{C}_2\text{O}_4$  (capture  $\text{h}^+$ ),  $\text{K}_2\text{Cr}_2\text{O}_7$  (capture  $\text{e}^-$ ), and ethanol (capture  $\bullet\text{OH}$ ) [49], were used to study their effects on catalyst performance. First, 10 mg of the catalyst and 50 mL of RhB solution (15 ppm) were mixed in the reaction vessel and stirred in the dark for 60 min to balance the adsorption-desorption, after which the scavenger was added, and this solution performed a photocatalytic reaction. The results (Fig. 9) showed that the addition of BQ significantly reduced the RhB degradation efficiency compared with the BiBTC@CNT catalyst. After 180 min, the decomposition efficiency decreased from 99 to 45%, indicating that BQ had a strong inhibitory effect on the activity of the material. Similarly, the addition of  $\text{K}_2\text{Cr}_2\text{O}_7$  slightly reduced the catalytic performance, with the decomposition efficiency decreasing from 99% to 90%. These results show that scavengers have a significant impact on the photocatalytic degradation of RhB, in which BQ has the strongest inhibitory effect, followed by  $\text{K}_2\text{Cr}_2\text{O}_7$ , and  $\text{Na}_2\text{C}_2\text{O}_4$  and Ethanol did not affect the activity and catalytic properties of the materials. The mechanism underlying the inhibitory effect of scavengers on the performance of the BiBTC@CNT catalyst is complex and depends on the specific scavenger used. For example,  $\text{Na}_2\text{C}_2\text{O}_4$  can act as an electron donor and compete

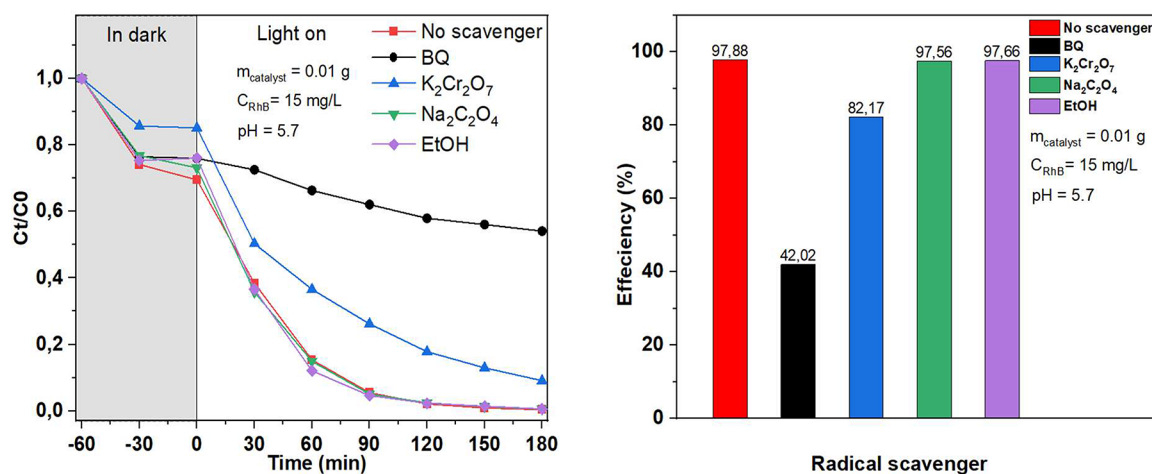
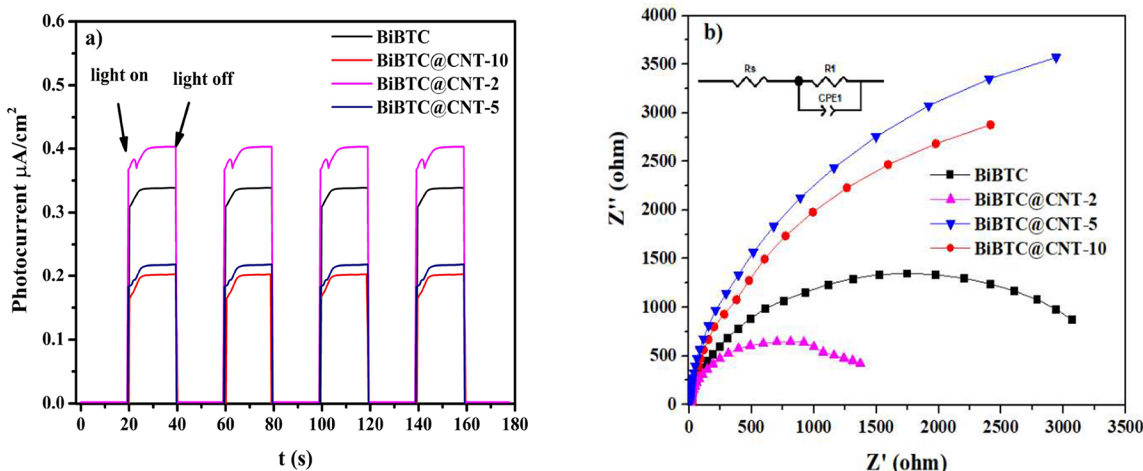


Fig. 9 Effects of different radical scavengers on the degradation of RhB

**Table 1** Some recent photocatalyst systems for photocatalyst degradation of RhB

Catalyst	wt% CNTs	Dyes	Concentration (ppm)	Lamp source	Efficiency, @Times (mins)	Ref
UiO-66-NH <sub>2</sub> @CNT	3	RhB	15	LED 100 W	93%@30 min	[46]
ZnO/CNTs	10	RhB	20	Sunlight	49%@ 60 min	[50]
g-C <sub>3</sub> N <sub>4</sub> /CNTs	1	RhB	10	Xenon 300 W	98.1%@60 min	[51]
g-C <sub>3</sub> N <sub>4</sub> /UU200	-	RhB	3	Sunlight	97.5%@ 90 min	[14]
Bi-BDC	-	RhB	14.4	visible LED light	99.44% %@ 360 min	[17]
BiBTC@CNTs	2	RhB	15	LED 60 W	98%@180 min	This study



**Fig. 10** (a) Transient photocurrent response and (b) EIS changes of BiBTC@CNTs-x

with RhB for the active sites on the catalyst surface, thereby hindering photocatalytic degradation. Overall, the results of this study demonstrate that the addition of free-radical scavengers can significantly affect the performance of the BiBTC@CNTs-2 catalyst in the photodegradation of RhB. Therefore, understanding the mechanism of free-radical inhibition can aid in the design of more efficient photocatalytic systems for wastewater treatment applications.

The BiBTC@CNTs-2 photocatalyst was assessed for its ability to degrade RhB dye by comparing it to other reported materials, as shown in Table 1. The results demonstrated that BiBTC@CNTs-2 exhibited significant potential as a photocatalyst for the degradation of RhB, particularly at higher dye concentrations and shorter processing times than Bi-MOFs (UU200 or Bi-BDC). This exceptional performance was attributed to the consistent distribution of Bi, O, and C elements, as well as the conductive CNTs in the BiBTC@CNTs microstructure.

### 3.1 Photoelectrochemical Performance

The separation and charge transfer performance of the BiBTC@CNTs-x catalyst were investigated using transient photocurrent response (Fig. 10a) and electrochemical impedance spectroscopy (EIS) (Fig. 10b). The light on and off times were 20 s during the testing of the transient

photocurrent. The results showed that the BiBTC@CNTs-2 composite had a larger photocurrent intensity (2.02 µA/cm<sup>2</sup>) than pure BiBTC (1.35 µA/cm<sup>2</sup>). According to previous studies [4, 52, 53], the separation efficiency of photo-generated charges is more effective, and the photocatalytic performance corresponds to a higher photocurrent intensity. The electrochemical impedance spectroscopy (EIS) results for the synthesized catalysts are presented in Fig. 11b. The corresponding equivalent circuit is shown in the top-right corner of the figure. A smaller semicircle radius reduces the charge-transfer resistance and enhances the carrier-transfer efficiency. Based on the specific resistance values, it is evident that BiBTC@CNTs-2 exhibits the lowest resistance, higher photocatalytic activity, and improved surface charge transfer ability compared to pure BiBTC. The effective separation and rapid transfer of e/h<sup>+</sup> pairs between BiBTC and CNT are responsible for this effect [54]. However, an increase in the weight% of carbon nanotubes (CNTs) prevents the active sites on the catalyst surface from contacting the solution. This phenomenon is commonly referred to as the shielding effect (SE).

### 3.2 Possible Photocatalytic Mechanism

To study the photocatalytic mechanism, the conduction and valence bands of BiBTC were analyzed using Mott–Schottky

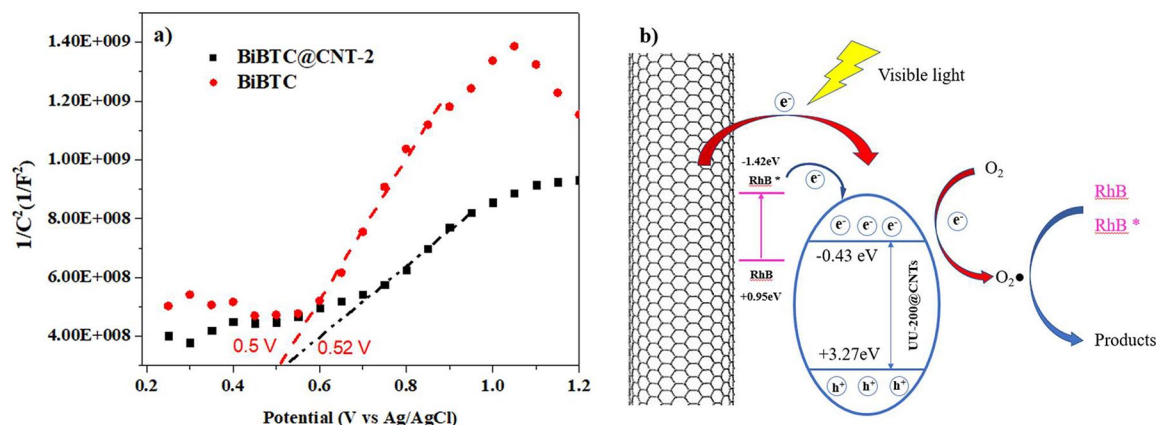


**Fig. 11** (a) Mott-Schottky plot of BiBTC and BiBTC@CNT-2 samples; and (b) degradation mechanism of RhB

plots (Fig. 11a). The positive slope of the curve for the BiBTC sample indicates that it is an n-type semiconductor. The flat-band potential of the semiconductor can be determined by the intersection of the fitted line with the X-axis; for BiBTC, it is  $-0.5$  eV (vs. Ag/AgCl). The minimum of the conduction band is approximately  $0.1$  V more negative than the flat-band potential of n-type semiconductors, so the conduction band potential value of BiBTC can be calculated to be  $-0.43$  eV (vs. NHE). By combining  $E_g$  (eV) and  $E_{CB}$ , the corresponding valence band edge potential was determined to be  $3.27$  eV, as shown in Fig. 11a. Furthermore, the shift in the slope of BiBTC@CNT-2 indicates an increase in the concentration of BiBTC electrons owing to electron transfer from the CNT to BiBTC. Figure 11b shows the RhB degradation mechanism. Previous investigations have found that MOF@CNT photogenerated electron-hole pairs when exposed to visible light [20, 38, 39]. Owing to their excellent electrical conductivity, CNT can avoid electron-hole pair recombination in the conduction band of BiBTC@CNT by capturing induced electrons ( $e^-$ ). Transferring electrons in the conduction band to the CNT reduces photogenerated electron-hole pair recombination and photocorrosion. The ideal BiBTC@CNT combination exhibited a greater photocatalytic dye breakdown efficiency than CNTs or BiBTC. Figure 11b shows that photoinduced electrons from RhB and CNT transfer to the conduction band (CB) of BiBTC, and these electrons of BiBTC CB are more negative than those of  $O_2/O_2^{\bullet-}$  ( $-0.33$  vs. NHE). Because photoinduced electrons in the MOF conduction band have a high reduction potential, they should react with oxygen molecules to form  $O_2^{\bullet-}$  [25, 39]. Meanwhile,  $OH/OH^-$  was less active than the valence band of BiBTC@CNTs. Thus, the holes in BiBTC cannot oxidize  $OH^-$  to generate  $OH^\bullet$  [38].

## 4 Conclusion

This study aimed to evaluate the efficacy of BiBTC@CNTs-x as a photocatalyst for RhB degradation. A microwave-assisted solvothermal process was employed to synthesize the BiBTC@CNT composite, which possesses the structure of UU-200 and CNT. The findings of the FESEM analysis indicate that the interwoven fibers of BiBTC and CNTs enhance the absorption of light energy and facilitate the separation of electron-hole pairs. This enhancement was demonstrated by the higher photocurrent intensity observed in BiBTC@CNTs-2 ( $2.02 \mu A/cm^2$ ) than in pure BiBTC ( $1.35 \mu A/cm^2$ ) and a smaller semicircle radius in the EIS results. The transfer of photoinduced electrons from CNTs to BiBTC was also observed through XPS and Mott-Schottky plots. The BiBTC@CNTs-2 material exhibited the best photocatalytic performance, with a complete decomposition of 97.88% RhB in 180 min. These findings demonstrate that CNTs significantly influence photocatalytic efficiency owing to their contribution to increased absorption in the visible light region and the extension of the lifetime of photogenerated electron-hole pairs. In addition, free radicals ( $\bullet O_2^-$ ) and electrons ( $e^-$ ) play crucial roles in the photodegradation of RhB.

**Supplementary Information** The online version contains supplementary material available at <https://doi.org/10.1007/s11244-024-01985-x>.

## References

- Lan D, Zhu H, Zhang J et al (2022) Adsorptive removal of organic dyes via porous materials for wastewater treatment in recent decades: a review on species, mechanisms and perspectives. *Chemosphere* 293
- Khairy M, Zakaria W (2014) Effect of metal-doping of TiO<sub>2</sub> nanoparticles on their photocatalytic activities toward removal

- of organic dyes. *Egyptian J Petroleum* 23:419–426. <https://doi.org/10.1016/j.ejpe.2014.09.010>
3. Nguyen TD, Nguyen VH, Pham ALH et al (2022) Fabrication of binary g-C<sub>3</sub>N<sub>4</sub>/UU-200 composites with enhanced visible-light-driven photocatalytic performance toward organic pollutant eliminations. *RSC Adv* 12:25377–25387
  4. Nguyen HP, Cao TM, Nguyen T-T, Pham V, Van (2023) Improving photocatalytic oxidation of semiconductor (TiO<sub>2</sub>, SnO<sub>2</sub>, ZnO)/CNTs for NO<sub>x</sub> removal. *J Ind Eng Chem.* <https://doi.org/10.1016/j.jiec.2023.07.017>
  5. Zheng M-W, Yang S-J, Pu Y-C, Liu S-H (2022) Mechanisms of biochar enhanced Cu<sub>2</sub>O photocatalysts in the visible-light photodegradation of sulfamethoxazole. *Chemosphere* 307:135984. <https://doi.org/10.1016/j.chemosphere.2022.135984>
  6. Liao M, Su L, Deng Y et al (2021) Strategies to improve WO<sub>3</sub>-based photocatalysts for wastewater treatment: a review. *J Mater Sci* 56:14416–14447. <https://doi.org/10.1007/s10853-021-06202-8>
  7. Van Pham V, La HPP, Le TQ et al (2023) Fe<sub>2</sub>O<sub>3</sub>/diatomite materials as efficient photo-Fenton catalysts for ciprofloxacin removal. *Environ Sci Pollut Res* 30:33686–33694. <https://doi.org/10.1007/s11356-022-24522-3>
  8. Ha Luu TV, Dao NN, Le Pham HA et al (2023) One-step hydrothermal preparation of Ta-doped ZnO nanorods for improving decolorization efficiency under visible light. *RSC Adv* 13:5208–5218. <https://doi.org/10.1039/d2ra07655a>
  9. Althamthami M, Guettaf Temam E, Ben Temam H et al (2022) Influence of hole-scavenger and different withdrawn speeds on photocatalytic activity of Co<sub>3</sub>O<sub>4</sub> thin films under sunlight irradiation. *Ceram Int* 48:31570–31578. <https://doi.org/10.1016/j.ceramint.2022.07.078>
  10. Teymourinia H, Rtimi S, Ghalkhani M et al (2023) Flower-like nanocomposite of carbon quantum dots, MoS<sub>2</sub>, and dendritic Ag-based Z-scheme type photocatalysts for effective tartrazine degradation. *Chem Eng J* 473:145239. <https://doi.org/10.1016/j.cej.2023.145239>
  11. Qin J, Pei Y, Zheng Y et al (2023) Fe-MOF derivative photocatalyst with advanced oxygen reduction capacity for indoor pollutants removal. *Appl Catal B* 325:122346. <https://doi.org/10.1016/j.apcatb.2022.122346>
  12. Sun D, Li Z (2017) Robust Ti- and Zr-Based Metal-Organic frameworks for Photocatalysis. *Chin J Chem* 35:135–147. <https://doi.org/10.1002/cjoc.201600647>
  13. Zaamouchi I, Kaci MM, Zidane Y et al (2024) The impressive photocatalytic performance of Zn-MOF as a novel photocatalyst for the effective purification of dyes under solar exposure. *J Mol Struct* 1299:137070. <https://doi.org/10.1016/j.molstruc.2023.137070>
  14. Nguyen TD, Nguyen VH, Le Hoang Pham A et al (2022) Fabrication of binary g-C<sub>3</sub>N<sub>4</sub>/UU-200 composites with enhanced visible-light-driven photocatalytic performance toward organic pollutant eliminations. *RSC Adv* 12:25377–25387. <https://doi.org/10.1039/d2ra04222c>
  15. Pham HA, Le, Nguyen DT, Nguyen VC, Ky Vo T (2024) Integrating bi-containing metal-organic frameworks for enhancing their LED visible-light-driven photocatalytic activities towards Rhodamine Dye. *Inorg Chem Commun* 159. <https://doi.org/10.1016/j.inoche.2023.111822>
  16. Nguyen VH, Van Tan L, Lee T, Nguyen TD (2021) Solvothermal synthesis and photocatalytic activity of metal-organic framework materials based on bismuth and trimesic acid. *Sustain Chem Pharm* 20. <https://doi.org/10.1016/j.scp.2021.100385>
  17. Nguyen VH, Nguyen TD, Van Nguyen T (2020) Microwave-assisted Solvothermal synthesis and photocatalytic activity of Bismuth(III) based metal-Organic Framework. *Top Catal* 63:1109–1120. <https://doi.org/10.1007/s11244-020-01271-6>
  18. Wang Q-X, Li G (2021) Bi(*μ*-scp) MOFs: syntheses, structures and applications. *Inorg Chem Front* 8:572–589. <https://doi.org/10.1039/D0QI01055C>
  19. Åhlén M, Kapaca E, Hedbom D et al (2022) Gas sorption properties and kinetics of porous bismuth-based metal-organic frameworks and the selective CO<sub>2</sub> and SF<sub>6</sub> sorption on a new bismuth trimesate-based structure UU-200. *Microporous Mesoporous Mater* 329. <https://doi.org/10.1016/j.micromeso.2021.111548>
  20. Pham HA, Le, Abd AA, Nguyen THA et al (2023) Optimization of photocatalytic degradation performance of organic dye using highly efficient bismuth MOFs: Preparation and parametric analysis. *Chem Eng Res Des* 198:196–207. <https://doi.org/10.1016/j.cherd.2023.08.040>
  21. Lin J, Ho W, Qin X et al (2022) Metal-Organic frameworks for NO<sub>x</sub> adsorption and their applications in separation, sensing, Catalysis, and Biology. *Small* 18. <https://doi.org/10.1002/sml.202105484>
  22. Chai W, Yin W, Wang K et al (2019) Carbon-coated bismuth nanospheres derived from Bi-BTC as a promising anode material for lithium storage. *Electrochim Acta* 325:134927. <https://doi.org/10.1016/j.electacta.2019.134927>
  23. Dong S, Wang L, Lou W et al (2023) Synthesis of TiO<sub>2</sub>/Bi-MOFs composites with excellent performance for enhanced visible-light driven photocatalytic activity to remove organic contaminants. *J Dispers Sci Technol* 44:2058–2069. <https://doi.org/10.1080/01932691.2022.2059503>
  24. Gao Y, Yi X-H, Wang C-C et al (2023) Effective Cr(VI) reduction over high throughput Bi-BDC MOF photocatalyst. *Mater Res Bull* 158:112072. <https://doi.org/10.1016/j.materresbull.2022.112072>
  25. Nguyen VH, Van Tan L, Lee T, Nguyen TD (2021) Solvothermal synthesis and photocatalytic activity of metal-organic framework materials based on bismuth and trimesic acid. *Sustain Chem Pharm* 20:100385. <https://doi.org/10.1016/j.scp.2021.100385>
  26. Qin H, Lv Y, Nakane K (2024) *In situ* growth of Bi-MOF on cotton fabrics via ultrasonic synthesis strategy for recyclable photocatalytic textiles. *RSC Adv* 14:11513–11523. <https://doi.org/10.1039/D4RA00493K>
  27. Yu F, Jin M, Zhang Y et al (2022) Visible-light-driven Zr-MOF/BiOBr heterojunction for the efficient synchronous removal of Hexavalent Chromium and Rhodamine B from Wastewater. *ACS Omega* 7:25066–25077. <https://doi.org/10.1021/acsomega.2c01298>
  28. Ahmad I, Akhtar MS, Ahmed E, Ahmad M (2020) Highly efficient visible light driven photocatalytic activity of graphene and CNTs based mg doped ZnO photocatalysts: a comparative study. *Sep Purif Technol* 245:116892. <https://doi.org/10.1016/j.seppur.2020.116892>
  29. Ghasemipour P, Fattahi M, Rasekh B, Yazdian F (2020) Developing the Ternary ZnO Doped MoS<sub>2</sub> nanostructures grafted on CNT and reduced Graphene Oxide (RGO) for photocatalytic degradation of Aniline. *Sci Rep* 10. <https://doi.org/10.1038/s41598-020-61367-7>
  30. Yang L, Xin Y, Yao C, Miao Y (2021) In situ preparation of Bi<sub>2</sub>WO<sub>6</sub>/CAU-17 photocatalyst with excellent photocatalytic activity for dye degradation. *J Mater Sci: Mater Electron* 32:13382–13395. <https://doi.org/10.1007/s10854-021-05917-3>
  31. Zhang F, Xiao X, Xiao Y, Cheng X (2023) Construction of novel 0D/2D AgI/CAU-17 heterojunction with excellent photocatalytic performance by in situ deposition-precipitation. *J Environ Chem Eng* 11. <https://doi.org/10.1016/j.jece.2023.109641>
  32. Zhang X, Xu Y, Ye B (2018) An efficient electrochemical glucose sensor based on porous nickel-based metal organic framework/carbon nanotubes composite (Ni-MOF/CNTs). *J Alloys Compd* 767:651–656
  33. Phin HY, Ong YT, Sin JC (2020) Effect of carbon nanotubes loading on the photocatalytic activity of zinc oxide/carbon nanotubes

- photocatalyst synthesized via a modified sol-gel method. *J Environ Chem Eng* 8. <https://doi.org/10.1016/j.jece.2019.103222>
34. Nguyen HP, Cao TM, Nguyen T et al (2023) Improving photocatalytic oxidation of semiconductor (TiO<sub>2</sub>, SnO<sub>2</sub>, ZnO)/CNTs for NO<sub>x</sub> removal. *J Ind Eng Chem*
  35. Deng P, Yang F, Wang Z et al (2020) Metal–Organic Framework-Derived Carbon Nanorods Encapsulating Bismuth Oxides for Rapid and Selective CO<sub>2</sub> electroreduction to Formate. *Angew Chem* 132:10899–10905
  36. Mwafy EA, Mostafa AM (2019) Multi walled carbon nanotube decorated cadmium oxide nanoparticles via pulsed laser ablation in liquid media. *Opt Laser Technol* 111:249–254. <https://doi.org/10.1016/j.optlastec.2018.09.055>
  37. Nguyen VH, Pham ALH, Nguyen VH et al (2022) Facile synthesis of bismuth(III) based metal-organic framework with difference ligands using microwave irradiation method. *Chem Eng Res Des* 177:321–330. <https://doi.org/10.1016/j.cherd.2021.10.043>
  38. Nguyen TD, Nguyen VH, Le Hoang Pham A et al (2022) Fabrication of binary g-C<sub>3</sub>N<sub>4</sub>/UU-200 composites with enhanced visible-light-driven photocatalytic performance toward organic pollutant eliminations. *RSC Adv* 12:25377–25387. <https://doi.org/10.1039/D2RA04222C>
  39. Pham HA, Le, Nguyen DT, Nguyen VC, Ky Vo T (2024) Integrating bi-containing metal–organic frameworks for enhancing their LED visible-light-driven photocatalytic activities towards Rhodamine Dye. *Inorg Chem Commun* 159:111822. <https://doi.org/10.1016/j.inoche.2023.111822>
  40. Guo M, Wang Y, He Q et al (2015) Enhanced photocatalytic activity of S-doped BiVO<sub>4</sub> photocatalysts. *RSC Adv* 5:58633–58639. <https://doi.org/10.1039/c5ra07603j>
  41. Liu S-H, Tang W-T, Chou P-H (2020) Microwave-assisted synthesis of triple 2D g-C<sub>3</sub>N<sub>4</sub>/Bi<sub>2</sub>WO<sub>6</sub>/rGO composites for ibuprofen photodegradation: kinetics, mechanism and toxicity evaluation of degradation products. *Chem Eng J* 387:124098. <https://doi.org/10.1016/j.cej.2020.124098>
  42. Zhao M, Meng L, Ma L et al (2018) Layer-by-layer grafting CNTs onto carbon fibers surface for enhancing the interfacial properties of epoxy resin composites. *Compos Sci Technol* 154:28–36. <https://doi.org/10.1016/j.compscitech.2017.11.002>
  43. Li H, Li Z, Wu Z et al (2019) Enhanced electrochemical performance of CuCo<sub>2</sub>S<sub>4</sub>/carbon nanotubes composite as electrode material for supercapacitors. *J Colloid Interface Sci* 549:105–113. <https://doi.org/10.1016/j.jcis.2019.04.056>
  44. de Menezes BRC, Ferreira FV, Silva BC et al (2018) Effects of octadecylamine functionalization of carbon nanotubes on dispersion, polarity, and mechanical properties of CNT/HDPE nanocomposites. *J Mater Sci* 53:14311–14327
  45. Jones TE, Rocha TCR, Knop-Gericke A et al (2015) Insights into the electronic structure of the oxygen species active in Alkene Epoxidation on Silver. *ACS Catal* 5:5846–5850. <https://doi.org/10.1021/acscatal.5b01543>
  46. Abdi J, Banisharif F, Khataee A (2021) Amine-functionalized Zr-MOF/CNTs nanocomposite as an efficient and reusable photocatalyst for removing organic contaminants. *J Mol Liq* 334. <https://doi.org/10.1016/j.molliq.2021.116129>
  47. Tuerdi A, Chen P, Zhao F et al (2013) In situ synthesis and photocatalytic property of bismuth nanocrystal-filled carbon tubes. *Chem Lett* 42:1279–1281. <https://doi.org/10.1246/cl.130563>
  48. Abdi J, Banisharif F, Khataee A (2021) Amine-functionalized Zr-MOF/CNTs nanocomposite as an efficient and reusable photocatalyst for removing organic contaminants. *J Mol Liq* 334:116129. <https://doi.org/10.1016/j.molliq.2021.116129>
  49. Truong TK, Van Doan T, Tran HH et al (2019) Effect of Cr Doping on visible-light-driven photocatalytic activity of ZnO nanoparticles. *J Electron Mater* 48:7378–7388
  50. Ahmad M, Ahmed E, Hong ZL et al (2014) Photocatalytic, sonocatalytic and sonophotocatalytic degradation of rhodamine B using ZnO/CNTs composites photocatalysts. *Ultrason Sonochem* 21:761–773. <https://doi.org/10.1016/j.ultsonch.2013.08.014>
  51. Liu G, Liao M, Zhang Z et al (2020) Enhanced photodegradation performance of rhodamine B with g-C<sub>3</sub>N<sub>4</sub> modified by carbon nanotubes. *Sep Purif Technol* 244. <https://doi.org/10.1016/j.seppur.2020.116618>
  52. Mai Tho NT, Van Cuong N, Luu Thi VH et al (2023) A novel n-p heterojunction Bi<sub>2</sub>S<sub>3</sub>/ZnCo<sub>2</sub>O<sub>4</sub> photocatalyst for boosting visible-light-driven photocatalytic performance toward indigo carmine. *RSC Adv* 13:16248–16259. <https://doi.org/10.1039/d3ra02803h>
  53. Nguyen SN, Truong TK, You SJ et al (2019) Investigation on photocatalytic removal of NO under visible light over Cr-Doped ZnO nanoparticles. *ACS Omega* 4:12853–12859. <https://doi.org/10.1021/acsomega.9b01628>
  54. Liu E, Du Y, Bai X et al (2020) Synergistic improvement of cr(VI) reduction and RhB degradation using RP/g-C<sub>3</sub>N<sub>4</sub> photocatalyst under visible light irradiation. *Arab J Chem* 13:3836–3848. <https://doi.org/10.1016/j.arabjc.2019.02.001>

**Publisher's Note** Springer Nature remains neutral with regard to jurisdictional claims in published maps and institutional affiliations.

Springer Nature or its licensor (e.g. a society or other partner) holds exclusive rights to this article under a publishing agreement with the author(s) or other rightsholder(s); author self-archiving of the accepted manuscript version of this article is solely governed by the terms of such publishing agreement and applicable law.